Materials Science & Engineering A 945 (2025) 148952

Contents lists available at ScienceDirect

Materials Science & Engineering A

journal homepage: www.elsevier.com/locate/msea

Effect of cooling rate after high-temperature heating on the ductility of 19Cr-0.020C-0.015N-0.4Nb stabilized ferritic stainless cast steel

Rie Nishio [a,b,*], Takuo Umetani [b], Yasuhiko Nakamura [c], Taisuke T. Sasaki [d], Akinobu Shibata [a,d]

[a] *Graduate School of Science and Technology, University of Tsukuba, 1-1-1, Tennodai, Tsukuba, Ibaraki, 305-8577, Japan*
[b] *Materials Development Group, HINODE Holdings Co., Ltd., Iwasaki, Harakoga, Miyaki-machi, Miyaki, Saga, 849-0101, Japan*
[c] *HINODE Casting & Metal Works Co., Ltd., 768-2, Narita, Nagai, Yamagata, 993-0075, Japan*
[d] *Research Center for Structural Materials, National Institute for Materials Science (NIMS), 1-2-1, Sengen, Tsukuba, Ibaraki, 305-0047, Japan*

ARTICLE INFO

Keywords:
Ferritic stainless cast steel
Nb stabilized steel
Heat treatment
Cooling rate
Ductility
Cleavage fracture

ABSTRACT

In as-cast material, cracking can occur during assembly or welding processes depending on the manufacturing conditions. This study proposed heat treatment strategies to improve the ductility of as-cast stabilized ferritic stainless cast steel containing Nb, particularly focusing on cooling rate after solution treatment. The specimen cooled at 1.0 °C/min (“Slow-cooled sample”) exhibited ductile fracture, while the specimen cooled at 2.0×10^4 °C/min (“Rapid-cooled sample”) exhibited low ductility and cleavage fracture. The fracture initiation site of the Rapid-cooled sample was a coarse oxide particle near the grain boundary. In the ferrite matrix surrounding the oxide particles in the Rapid-cooled sample, more dislocations were observed compared to the Slow-cooled sample. These dislocations are likely introduced by local thermal stress generated during rapid cooling, resulting in the suppression of plastic accommodation around the oxide particles during plastic deformation. Consequently, stress concentration at the crack tips of the oxide particles and their Nb(C, N) coating increases, causing the cracks to propagate into the ferrite matrix. Accordingly, we concluded that the dislocations introduced around the oxide particles are one of the major factors reducing the ductility of the Rapid-cooled sample.

1. Introduction

Ferritic stainless steel is widely used in heat-resistant applications due to its low thermal expansion coefficient, excellent high-temperature corrosion resistance, and cost-effectiveness resulting from the absence of Ni additions [1–5]. Among them, stabilized ferritic stainless steel with Nb addition possesses high corrosion resistance, heat resistance, and weldability, making it suitable for automotive exhaust components and welded structures [6–12]. These properties are attributed to the fact that Nb preferentially forms carbides or nitrides over Cr, thereby preventing the reduction in corrosion resistance caused by grain boundary precipitation of $Cr_{23}C_6$ [13–16].

In recent years, automotive exhaust components made of stabilized ferritic stainless steel have become increasingly complex in shape and lighter in weight due to stricter environmental regulations. In addition, there is a demand for reducing manufacturing costs and eliminating processing steps such as rolling and forging. To meet these requirements, investment casting method has been adopted for their production. Casting methods generally allow for the production of single-piece components with complex shapes and offer excellent recyclability. Particularly, the investment casting method enables the production of thin-walled castings with high dimensional accuracy by heating the mold, making it suitable for automotive exhaust components [17–19].

On the other hand, it is well known that castings generally exhibit inferior mechanical properties, particularly ductility and toughness, compared to rolled or forged materials. The main factors are coarse grain size, microsegregation during solidification, precipitation of brittle phases caused by segregation, and precipitation of compound phases during the cooling process after solidification [20–25]. In stabilized ferritic stainless cast steel, as-cast material with insufficient ductility may develop cracking during assembly or welding processes, depending on the manufacturing conditions. Therefore, improving the ductility of these cast steel in the as-cast condition is essential. We previously investigated the microstructure and mechanical properties of stabilized ferritic stainless cast steel containing 19 wt% Cr, 0.020 wt% C, and 0.015 wt% N, with the Nb content varied in the range of 0.2 wt% to 1.0

---

* Corresponding author. Graduate School of Science and Technology, University of Tsukuba, 1-1-1, Tennodai, Tsukuba, Ibaraki, 305-8577, Japan.
E-mail address: s2336005@u.tsukuba.ac.jp (R. Nishio).

https://doi.org/10.1016/j.msea.2025.148952
Received 1 May 2025; Received in revised form 5 August 2025; Accepted 11 August 2025

wt%. We found that, as the Nb content increased, Nb became enriched in the final solidification zone, leading to the formation of a brittle eutectic structure as well as the precipitation of coarse Nb(C, N) and Laves-phases along the grain boundaries, resulting in a significant decrease in ductility. From the perspectives of corrosion resistance and ductility, we identified the appropriate Nb content is 0.35–0.45 wt% [26]. However, even with the appropriate Nb content, the average elongation of the as-cast material was 5 %–10 %, indicating that further improvement in ductility is essential to prevent cracking during secondary processing.

High-temperature heat treatment is often applied to cast steel products in order to improve their mechanical properties [27–30]. Zhao et al. [31] conducted a systematic heat treatment study on a low-carbon microalloyed cast steel containing Nb, Ti, and V by varying the holding temperature in the range of 950 °C–1200 °C. They found that heat-treated material, which exhibited significantly higher ductility and toughness than as-cast material, had a uniform pearlite structure. They consider that this microstructural change was caused by the mitigation of carbon microsegregation through heat treatment. Xie et al. [32] conducted a heat treatment study on an austenitic stainless cast steel containing 0.9 wt% Nb and reported that tensile strength and elongation were significantly improved by homogenization at temperatures above 1150 °C–1250 °C for 5 h. They consider that the improvement in mechanical properties is due to the dissolution of eutectic NbC continuously crystallized in the as-cast material, resulting in the suppression of crack propagation along the eutectic NbC. These findings indicate that optimizing heat treatment conditions in cast steel is effective in improving mechanical properties by mitigating microsegregation and controlling the distribution of compounds.

In the case of Nb-stabilized ferritic stainless cast steel, heat treatment is sometimes empirically applied in industrial practice, and several studies reported its effects on microstructural changes and mechanical properties. Hu et al. [33] reported that heat treatment at 800 °C–850 °C for 1–3 h on a ferritic stainless cast steel containing 0.44 wt% Nb reduced the variation in elongation; while the as-cast specimens showed a wide range from 4.0 % to 27.6 %, the heat-treated specimens exhibited a narrower range of 22.4 %–26.5 %. They consider that the reduction in the variation of elongation is due to the fine and uniform precipitation of the Laves-phase by heat treatment. Kang et al. [34] reported that annealing at 850 °C for 2 h improved the ductility of a ferritic stainless cast steel containing 0.24 wt% Nb. They consider that the improvement resulted from the mitigation of stress concentration during deformation, which was caused by the transformation of coarse Nb(C, N) precipitates, originally located along grain boundaries in the as-cast condition, into more sparsely distributed granular particles through heat treatment. These studies focus on the optimization of holding temperature and holding time during the heat treatment, and provide important insights into improving ductility through the control of precipitates. On the other hand, the microstructure of Nb-stabilized ferritic stainless cast steel contains a large number of Nb(C, N) precipitates and deoxidation products, which are uniformly distributed throughout the material and differ significantly in physical properties from the ferrite matrix. Therefore, depending on the cooling conditions in heat treatment, the microstructure may change due to the stress introduced around the compounds, potentially leading to variations in mechanical properties. We considered that investigating the microstructural changes associated with the cooling rate after high-temperature holding of as-cast material could lead to the establishment of simple and effective heat treatment strategies to improve mechanical properties, particularly ductility. This study investigated the effects of cooling rates after high-temperature holding on the microstructure and mechanical properties of as-cast stabilized ferritic stainless cast steel containing Nb, and discussed the factors influencing ductility by analyzing fracture modes, crack propagation behavior, and microstructures in detail.

2. Experimental

The raw materials used in this study were ferritic stainless steel scrap, ferro-chrome, ferro-manganese, ferro-silicon, and ferro-niobium. The nominal chemical composition was Cr: 19, C: 0.020, N: 0.015, Nb: 0.4, P: 0.03, S: 0.01, Cu: 0.5, Si: 0.5, Mn: 0.12, and Fe: balance (wt%). The cast specimens were prepared by melting the raw materials at 1680 °C in a high-frequency induction furnace and casting the molten metal into sand molds to produce rod-shaped specimens with a diameter of 25 mm and length of 250 mm. The cast specimens were held at 1100 °C for 3 h in an argon atmosphere, then cooled to room temperature at various rates ranging from 2.0×10^4 °C/min to 1.0 °C/min by oil quenching, boiling water quenching, natural air cooling, forced air cooling and furnace cooling. The cooling rates were calculated based on the temperature measured using a thermocouple fixed to the side of the specimen in the range from 1100 °C to 80 °C. A K-type thermocouple with a wire diameter of 1.6 mm (Sanko: T-35) and a data logger (KEYENCE: TR-V550) were used for the measurement, with a sampling rate of 2 samples/sec. According to a phase diagram calculated using the thermodynamic software Thermo-Calc (database: Thermo Tech TCFE9) [35], Nb(C, N) precipitated through stabilization is fully dissolved in the ferrite matrix at 1327 °C. However, considering severe oxidation at that temperature, the heat treatment temperature was set to 1100 °C to ensure productivity.

Microstructure observations were conducted on the specimen cooled at a rate of 2.0×10^4 °C/min by oil quenching (referred to as the “Rapid-cooled sample”) and the specimen cooled at a rate of 1.0 °C/min in a furnace (referred to as the “Slow-cooled sample”). The specimen surfaces were prepared by sequential polishing with wet abrasive papers, diamond paste, colloidal silica suspension, and finished with ion milling (Hitachi High-Tech: IM4000 PLUS Ion Milling System). Observations were performed using field-emission scanning electron microscopy (FE-SEM, JEOL: JSM-IT800SHL) at an acceleration voltage of 5 kV. To identify the second-phase particles, elemental mapping was performed using energy-dispersive X-ray spectroscopy (EDS) on the Rapid-cooled sample. The measurements and analysis were conducted with an EDS detector (AMETEK: Octane Elect) attached to the FE-SEM, using AMETEK EDAX APEX EDS software. The acceleration voltage was 10 kV, and the working distance was 10 mm. In the EDS measurements, the following characteristic X-ray lines were used: C-Kα, N-Kα, O-Kα, Al-Kα, Si-Kα, Cr-Kα, Mn-Kα and Nb-Lα. The size and number density of Nb(C, N) precipitates, as well as the diameter of oxide particles formed as deoxidation products were measured using SEM-BSE images taken over a 3 mm^2 area including grain boundaries, analyzed with image processing software (Inotech: Quick grain). To quantify the thickness and coverage rate of Nb(C, N) formed around the oxide particles, 50 oxide particles were randomly selected from each sample, and measurements were conducted using SEM-BSE images. The thickness of Nb(C, N) was measured at areas where the coating was continuous and uniform along the surface of the oxide particles. The coverage rate of Nb(C, N) was evaluated as the ratio of the Nb(C, N)-covered perimeter to the total perimeter of the oxide particle. The morphology of oxide particles coated with Nb(C, N) was observed by FE-SEM after deep-etching in vilella reagent (1 g of picric acid, 5 ml hydrochloric acid, 100 ml ethanol) for 4 h.

Mechanical properties were evaluated through uniaxial tensile test at room temperature using a universal testing machine (Shimadzu Scientific Instruments: UH-300kNC), according to JIS Z 2241 (ISO 6892-1). The dimensions of test pieces were a gauge diameter of 8 mm and gauge length of 44 mm. The displacement rate was 0.7 mm/min until the stress exceeded the 0.2 % proof stress, followed by 5.0 mm/min. The fracture surfaces of the Rapid-cooled and Slow-cooled samples were observed using optical microscopy (OM, KEYENCE: VHX-7000) and FE-SEM at an acceleration voltage of 5 kV. A cross-section normal to the fracture surface of the Rapid-cooled sample was polished and ion milled in the same manner as the microscopic observation sample, and

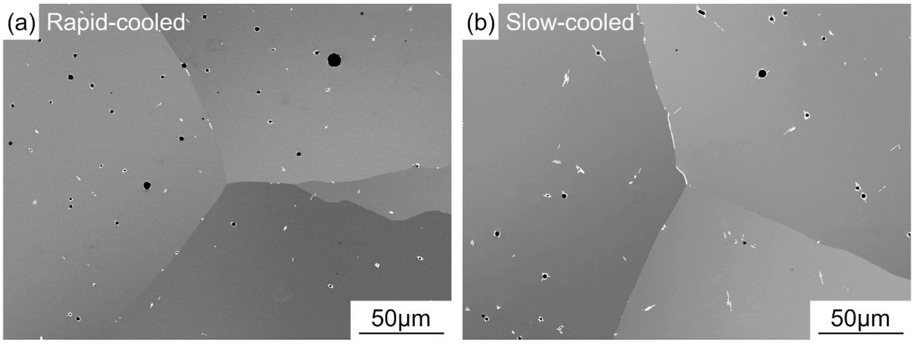

Fig. 1. SEM-BSE images of the (a) Rapid-cooled sample and (b) Slow-cooled sample.

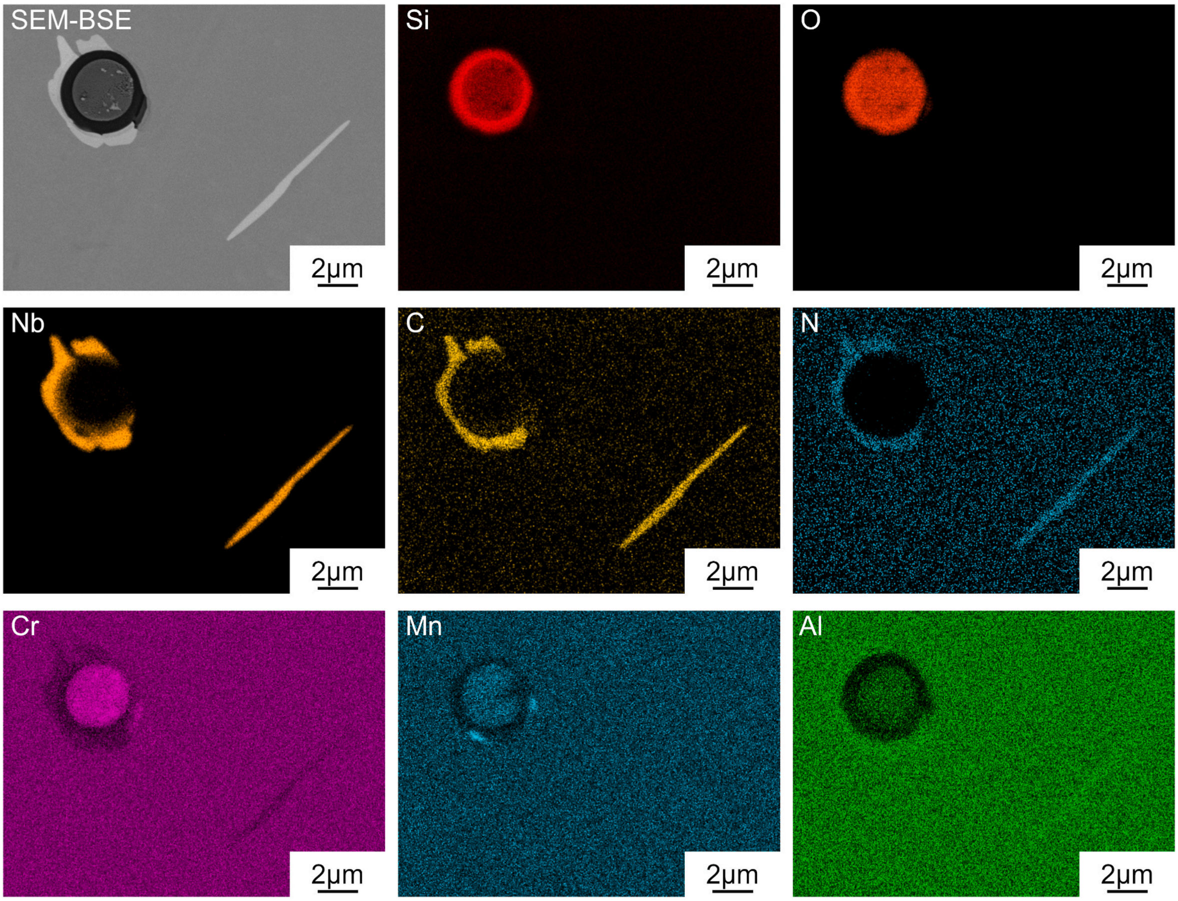

Fig. 2. EDS mapping of the precipitated particles in the Rapid-cooled sample.

analyzed for crystallographic orientation using electron backscatter diffraction (EBSD) system. EBSD mapping was performed using an EBSD detector (AMETEK: Orion Super) and analysis software (AMETEK: EDAX OIM Analysis 8) attached to the FE-SEM at an acceleration voltage of 15 kV, working distance of 15 mm and step size of 15 μm. In the EBSD analysis of this study, the angle difference between adjacent measurement points was classified as low-angle grain boundaries (LAGBs) in the range of 2–15° and high-angle grain boundaries (HAGBs) in the range of 15° or more. Angle differences of less than 2° were considered to fall within the measurement error range and were not regarded as grain boundaries. Phase indexing was conducted using the CIF file of bcc-Fe.

To investigate the initiation and propagation behavior of cracks, the cross-sections along the tensile direction of specimens unloaded at 10 % strain for the Rapid-cooled and Slow-cooled samples were observed using FE-SEM at an acceleration voltage of 5 kV and 15 kV. EBSD measurements of the Rapid-cooled sample were performed at an acceleration voltage of 15 kV, with a working distance of 15 mm and step size of 50 nm for areas containing oxides of 20 μm × 25 μm, and with a working distance of 20 mm and step size of 30 μm for wide areas of 10 mm × 23 mm.

Nanohardness measurements were performed on the polished surface of the Rapid-cooled and Slow-cooled samples, which were prepared following the above-described procedures. Mechanically and ion polished specimens were used because the surface of electrolytically polished specimens exposed second-phase particles, making it difficult to measure the target areas. In order to avoid the scattering of nanohardness values depending on crystal orientation, the grains with a normal direction close to <0 1 1> were selected for the measurements. Nanoindentation tests were conducted at room temperature under load control (Bruker: Hysitron Tribo Indenter TI950). A Berkovich diamond

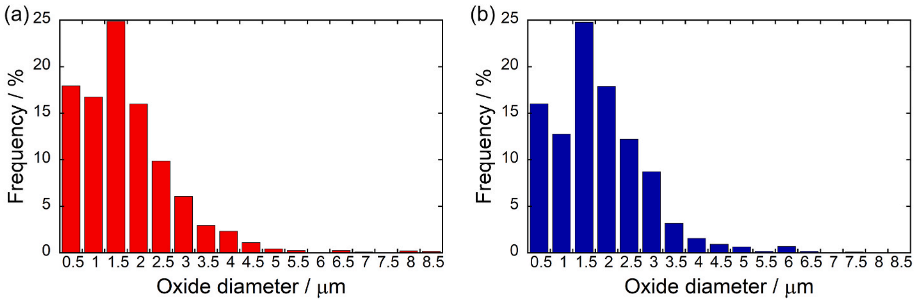

Fig. 3. Frequency distribution of the oxide diameters for the (a) Rapid-cooled sample and (b) Slow-cooled sample.

Table 1
Size and distribution for oxide particles and plate-like Nb(C, N).

Sample	Oxide particle			Intragranular Nb(C, N)			Grain boundary Nb(C, N)	
	Avg. diameter (μm)	Max. diameter (μm)	Number density (/mm^2)	Avg. length (μm)	Max. length (μm)	Number density (/mm^2)	Avg. length (μm)	Max. length (μm)
Rapid-cooled	2.0±0.04	11.2	617	1.8±0.9	3.9	505	1.6±1.3	7.0
Slow-cooled	2.1±0.08	13.6	604	2.6±1.4	10.8	465	4.3±3.3	15.7

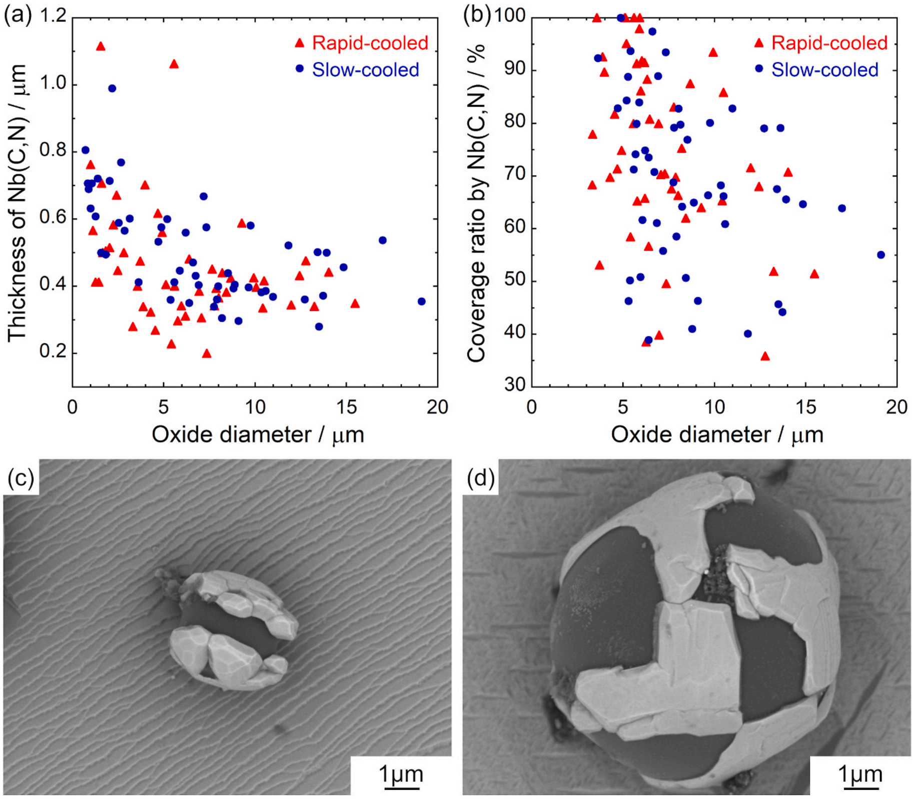

Fig. 4. (a, b) Relationship between the oxide diameter, the thickness of Nb(C, N), and the coverage ratio by Nb(C, N). (c, d) SEM-BSE images of the oxide coverage by Nb(C, N) in the Rapid-cooled sample after deep etching.

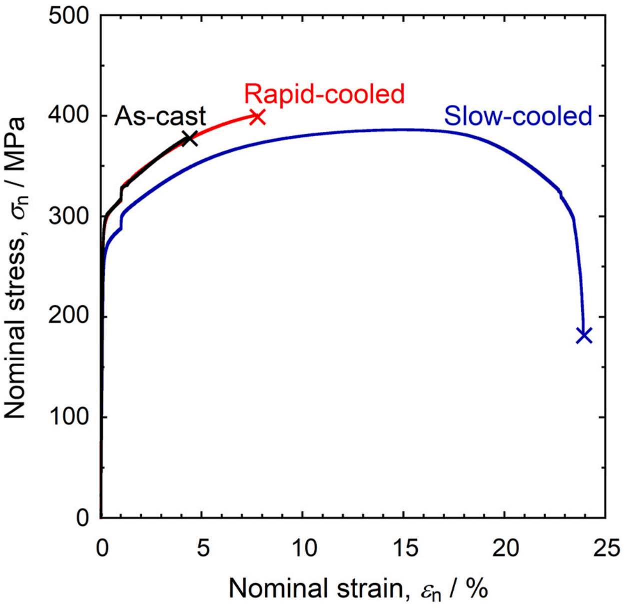

Fig. 5. Nominal stress-strain curves of the As-cast sample, Rapid-cooled sample, and Slow-cooled sample.

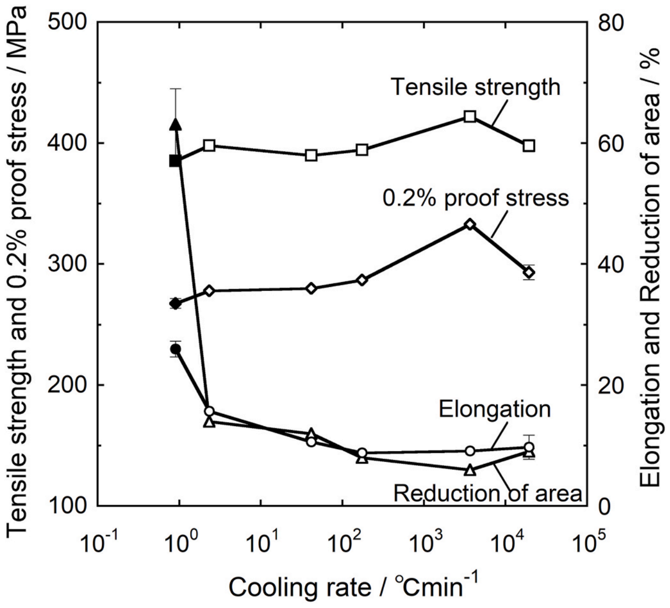

Fig. 6. Relationship between cooling rate and mechanical properties after heat treatment of as-cast specimen. The open markers indicate a ductile fracture surface ratio less than 10 %, while the filled markers indicate a ductile fracture surface ratio more that 80 %.

indenter was used with a maximum load of 1000 μN, a loading/unloading rate of 50 μN/s, and a holding time of 10 s at the maximum load.

The ferrite matrix of the Rapid-cooled and Slow-cooled samples were observed using scanning transmission electron microscopy (STEM, Thermo Fisher Scientific: Titan G2 80–200). Thin-film specimens for high-angle annular dark field (HAADF)-STEM were prepared using a focused ion beam (FIB, Thermo Fisher Scientific: Helios G4). The dislocation density was measured from the images taken by exciting the diffraction vector of $g^* = 0\ 0\ 2$. The specimen thickness of the observed area was determined using electron energy loss spectrometry (EELS) with STEM (JEOL: JEM-2800).

3. Results

Fig. 1 presents backscattered electron images observed using SEM (SEM-BSE images) of the (a) Rapid-cooled sample and (b) Slow-cooled sample. Both samples consist of a single-phase ferrite matrix. The average grain size is 2.0 mm for the Rapid-cooled sample and 2.2 mm for the Slow-cooled sample. Fig. 2 shows the results of EDS mapping performed on the second-phase particles of the Rapid-cooled sample. The spherical inclusions with the darkest contrast in the SEM-BSE image are Si-rich oxides. The gray regions at the core of the Si oxides contained Cr, Mn, Al, and O, indicating that they are complex oxides consisting of these elements. These inclusions are referred to as the "oxide particles". The oxide particles originated from deoxidizers added during the casting process, and they were generated in the molten metal. The precipitates observed with brighter contrast than the ferrite matrix in Fig. 1 and SEM-BSE image of Fig. 2 correspond to Nb(C, N), which precipitated during the cooling process after solidification. The Nb(C, N) nucleated on oxide particles or MnS, approximately 100 nm in size, and either grew into a plate-like shape or coated the oxide particles.

Table 1 summarizes the sizes of oxide particles and plate-like Nb(C, N) in the Rapid-cooled and Slow-cooled samples. Fig. 3 shows the diameter distribution of the oxide particles. The oxide particles measured include both those coated with Nb(C, N) and those uncoated. The average diameter and number density of oxide particles do not differ significantly depending on the cooling rate, as shown in Table 1. Similarly, Fig. 3(a, b) indicates that the frequency distribution of oxide particle sizes is comparable. On the other hand, the average length of plate-like Nb(C, N) is longer in the Slow-cooled sample for both grain interiors and grain boundaries, and the number density of plate-like Nb (C, N) in the grain interior is slightly lower in the Slow-cooled sample. Fig. 4(a, b) show the thickness of the Nb(C, N), and the coating coverage rate as a function of the diameter of oxide particles coated with Nb(C, N). A total of 50 oxide particles were randomly selected from each sample for measurement. Fig. 4(c, d) show SEM-BSE images of the Rapid-cooled sample after deep etching, demonstrating the coating of oxide particles by Nb(C, N). For both samples, as depicted in Fig. 4(a, b), the thickness of the Nb(C, N) coating and the coating coverage rate decrease as the oxide particle diameter increases. The area fraction of Nb (C, N) measured over a 3 mm^2 region, including grain boundaries, was 0.4 % for the As-cast sample, 0.3 % for the Rapid-cooled sample, and 0.5 % for the Slow-cooled sample.

Fig. 5 shows the nominal stress-nominal strain curves of the As-cast, Rapid-cooled, and Slow-cooled samples. While the total elongation of the As-cast sample is 4.3 %, the Rapid-cooled sample exhibits a higher value of 7.7 %, although it fractured within the uniform elongation regime. In contrast, the Slow-cooled sample shows significantly larger uniform elongation than both the As-cast and Rapid-cooled samples and sufficient local elongation before final ruputure. We should note that the total elongation of the Slow-cooled sample is 23.9 %, approximately three times higher than that of the Rapid-cooled sample.

Fig. 6 shows the relationship between cooling rate and mechanical properties; open and solid markers indicate a ductile fracture surface ratio of less than 10 % and more than 80 %, respectively. The plotted values for the Rapid-cooled sample (cooling rate: 2.0×10^4 °C/min) and the Slow-cooled sample (cooling rate: 1.0 °C/min) represent the average of five measurements with error bars. For the samples with intermediate cooling rates, the values represent the average of two measurements. Tensile strength and 0.2 % proof stress tend to increase slightly with an increase in cooling rate. On the other hand, elongation and reduction of area increase with decreasing cooling rate. They increase significantly when the cooling rate is below 10 °C/min, accompanied by a higher ductile fracture surface ratio. The results presented in Figs. 5 and 6 demonstrate that the mechanical properties of the cast steel vary significantly with heat treatment. More specifically, slower cooling rates after high-temperature holding markedly improve ductility.

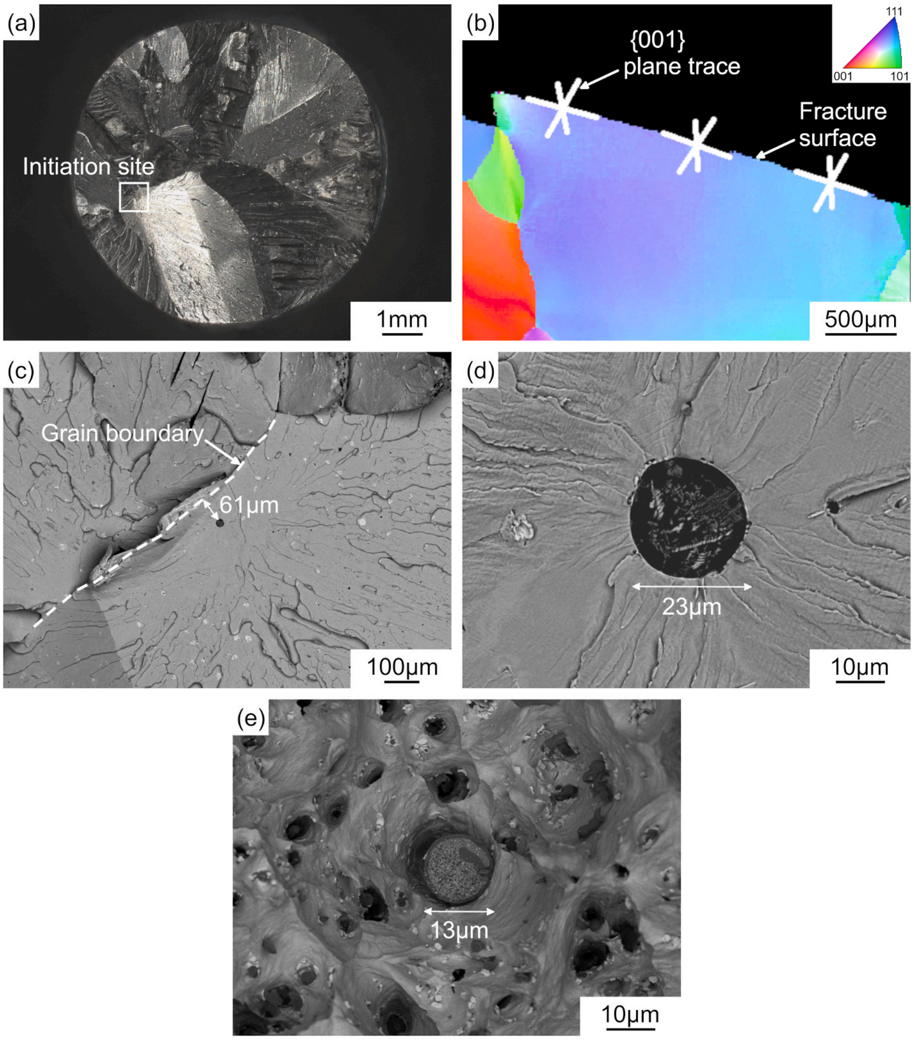

Fig. 7. (a) Optical microscopy image of the fracture surface for the Rapid-cooled sample. (b) IPF map of a cross-section normal to a fracture surface of the Rapid-cooled sample, which is different from shown in (a). (c, d) SEM-BSE images of the fracture initiation site for the Rapid-cooled sample shown in (a). (e) SEM-BSE image of the fracture surface for the Slow-cooled sample.

Fig. 7(a) shows an optical microscopy image of the fracture surface of the Rapid-cooled sample. The fracture surface consists of approximately 1–2 mm facets. Fig. 7(b) shows an Inverse Pole Figure (IPF) map obtained using EBSD on a cross-section normal to the fracture surface of a different Rapid-cooled sample than that shown in Fig. 7(a). The white lines indicate traces of the {0 0 1} planes, which are typical cleavage planes in body-centered cubic crystal, and they were nearly parallel to the fracture surface. This indicates that the Rapid-cooled sample exhibited cleavage fracture. The region enclosed by a rectangle in Fig. 7(a) marks the fracture initiation site identified from the morphology of the river patterns on the fracture surface, with its SEM-BSE image shown in Fig. 7(c). The dashed white lines in Fig. 7(c) correspond to boundary between facets, interpreted as grain boundary. The distance between the fracture initiation site, where river patterns converge, and the grain boundary is 61 μm. Because the average grain size of the Rapid-cooled sample is 2.0 mm, the fracture initiation site can be regarded as near the grain boundary. The SEM observations revealed no intergranular fracture or ductile fracture on the fracture surface of the Rapid-cooled sample. Fig. 7(d) shows a high-magnification SEM-BSE image of the fracture initiation site in the Rapid-cooled sample, where a crack initiated at an oxide particle and propagated radially through the ferrite matrix. While the average diameter of oxide particles in the sample is 2.0 μm, as shown in Table 1, the oxide particle at the fracture initiation site was significantly larger (~23 μm). The slightly brighter contrast within the oxide particle corresponds to a core of Cr, Mn, and Al complex oxides surrounded by Si oxide. The observation of this core suggests that the oxide particle was also fractured. Moreover, voids cannot be observed at the interface between the oxide particle and the ferrite matrix. Therefore, we can conclude that the cracks formed within the coarse oxide particles located near the grain boundaries or at their interface with the ferrite matrix in the Rapid-cooled sample. Fig. 7(e) shows the SEM-BSE image of the fracture surface of the Slow-cooled sample. Although a broken coarse oxide particle with a diameter of 13 μm can be observed, the fracture surface of the Slow-cooled sample shows dimples in contrast to the Rapid-cooled sample, indicating that it exhibited ductile fracture.

To investigate the initiation and propagation behavior of cracks in more detail, we observed the cross-sections along the tensile direction of specimens unloaded at 10 % strain for the Rapid-cooled and Slow-cooled samples. As shown in Fig. 8(a), the oxide particles and the Nb(C, N) coating are cracked in the Rapid-cooled sample, with the cracks propagating into the ferrite matrix. Fig. 8(b) shows an IPF map of the same area as Fig. 8(a). The white lines represent traces of the {0 0 1} planes of body-centered cubic crystal. These lines align with the crack traces that propagated through the ferrite matrix, confirming the occurrence of cleavage cracks in the Rapid-cooled sample. Interestingly, as shown in Fig. 8(c), oxide particles not coated with Nb(C, N) were not fractured but formed voids at the interface with the ferrite matrix. Generally, the

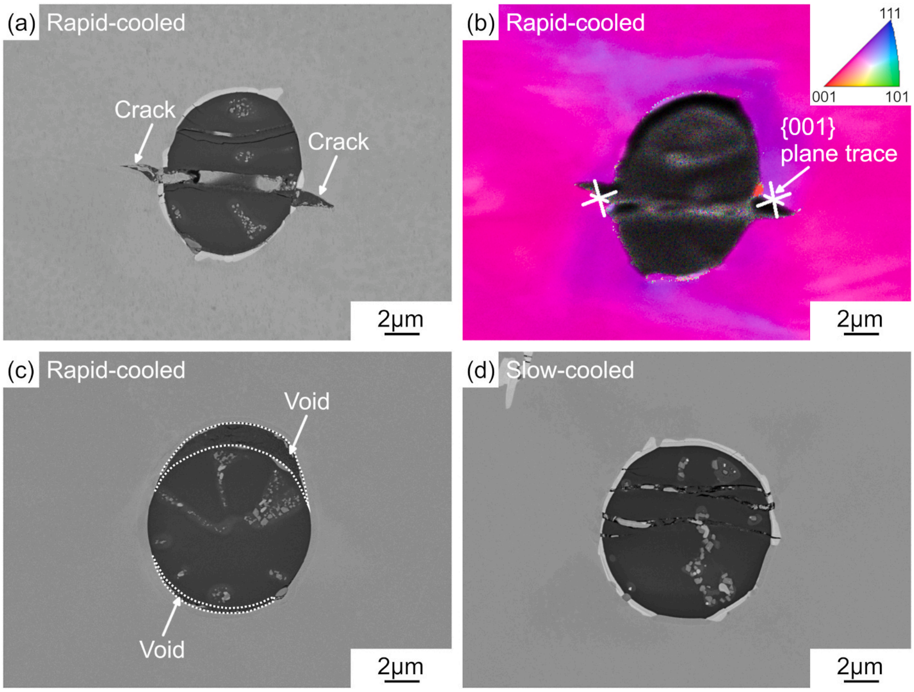

Fig. 8. SEM-BSE images of the cross section along the tensile direction of the sample unloaded at $\varepsilon = 10$ % for the (a, c) Rapid-cooled sample and (d) Slow-cooled sample. (b) IPF map for same field as (a). The tensile direction is vertical in the images.

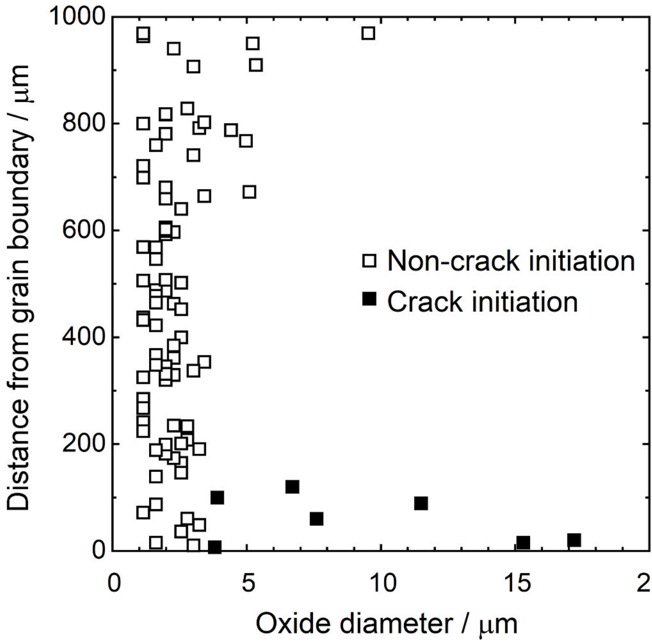

Fig. 9. Relationship between the oxide diameter and the distance from the grain boundary in the Rapid-cooled sample unloaded at 10 % strain.

fracture of second-phase particles during deformation can be attributed to stress concentration around the particles, caused by differences in the extent of plastic deformation between the surrounding matrix and the second-phase particles, which leads to inhomogeneous plastic strain [36–39]. In this cast steel, Nb(C, N) and oxide particles are significantly harder and more brittle than the ferrite matrix. Therefore, during the plastic deformation process, Nb(C, N) and oxide particles become more prone to fracture due to the increased plastic strain in their surrounding areas. On the other hand, the incoherency of interface between the matrix and second-phase particles usually leads to delamination when the applied stress exceeds the bonding strength [40–43]. The Nb(C, N) precipitates satisfy the Baker-Nutting orientation relationship with respect to the ferrite matrix ($(1\ 0\ 0)_{\mathrm{Nb(C,\ N)}}//(1\ 0\ 0)_{\mathrm{Fe}}$, $[0\ 1\ 0]_{\mathrm{Nb(C,\ N)}}//[0\ 1\ 1]_{\mathrm{Fe}}$, $[0\ 0\ 1]_{\mathrm{Nb(C,\ N)}}//[0\ \bar{1}\ 1]_{\mathrm{Fe}}$), ensuring crystallographic compatibility due to their common cubic crystal system [26]. In contrast, the oxide particles, being amorphous, have no crystallographic coherence with the ferrite matrix. Therefore, we infer that the oxide particles not coated with Nb(C, N) exhibited delamination at the interface with the ferrite matrix before fracture. In the Slow-cooled sample, as shown in Fig. 8(d), the oxide particles and their surrounding Nb(C, N) coatings were cracked, but no cracks propagating through the ferrite matrix were observed.

In the Rapid-cooled sample unloaded at 10 % strain, multiple cleavage cracks in the ferrite matrix initiated from oxide particles coated with Nb(C, N) were observed, as shown in Fig. 8(a). Fig. 9 shows the diameters of the oxide particles at the crack initiation sites and their distances from grain boundaries, plotted as black squares. For comparison, the oxide particles that did not act as crack initiation sites, randomly selected within a 100 μm × 1000 μm region in the grain, were plotted as white squares in Fig. 9. It is evident that the oxide particles acting as initiation sites for cleavage cracks in the ferrite matrix of the Rapid-cooled sample were coarser and located closer to the grain boundaries compared to the oxide particles that did not act as crack initiation sites. Fig. 10 shows the Kernel Average Misorientation (KAM) map of the Rapid-cooled sample unloaded at 10 % strain obtained by EBSD. KAM indicates the average local misorientation, calculated using orientation data from the first-nearest neighboring point around each measurement location. The locations of oxide particles that acted as initiation sites for cleavage cracks are indicated by black arrows. We found that the cleavage cracking occurred in the regions with high KAM values, suggesting that the cleavage cracks were generated in areas with high local strain levels. Fig. 11 shows the SEM-BSE images of the (a, b) undeformed samples and (c, d) unloaded at 10 % strain samples for the Rapid-cooled and Slow-cooled samples. The white dashed lines indicate the position of grain boundaries. In both samples, the undeformed ferrite matrix exhibited uniform contrast within individual grains, whereas the deformed ferrite matrix showed distinct channeling contrast. Local

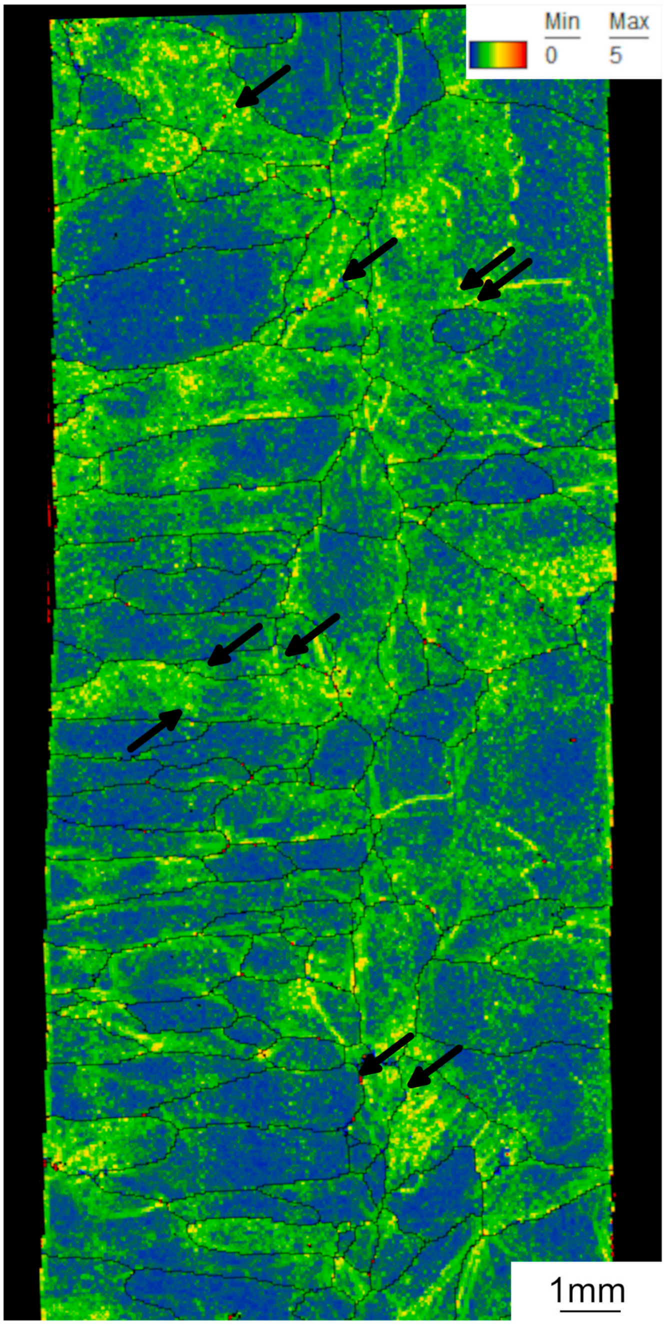

Fig. 10. KAM map of the Rapid-cooled sample unloaded at 10 % strain of the cross section along the tensile direction. The tensile direction is vertical in the map. The black lines indicate HAGBs, and the black arrows indicate the location of cleavage cracks.

deformation occurred in the vicinity of grain boundaries during deformation, regardless of the cooling rate. However, the Rapid-cooled sample exhibited cleavage cracks in the ferrite matrix, whereas no cleavage crack was observed in the Slow-cooled sample. Based on the observations presented above, we have clarified the deformation process of the Rapid-cooled sample as follows: Coarse oxide particles coated with Nb(C, N), located in the regions of high local strain near grain boundaries, are cracked. Subsequently, the cracks propagate along the cleavage planes of the ferrite matrix, originating from these oxide particles. Furthermore, when sufficiently high local stress concentrations develop, the cleavage cracks propagate, ultimately leading to brittle fracture. In contrast, in the Slow-cooled sample, while local deformation in the ferrite matrix and fracture of oxide particles coated with Nb(C, N) occur, the cracks do not propagate into the ferrite matrix, resulting in ductile fracture.

4. Discussion

The factors affecting ductility include: (i) the size and volume fraction of oxide particles, (ii) the thickness and coverage rate of Nb(C, N) on oxide particles, and (iii) higher dislocation density around the oxide particles. The size and number density of plate-like Nb(C, N) differ between the Rapid-cooled and Slow-cooled samples, as shown in Table 1. However, based on the observations so far, we have confirmed that it does not act as a crack initiation site, suggesting that its contribution to ductility is minimal. In the following, we discuss the effects of factor (i) to (iii).

4.1. The size and volume fraction of oxide particles

In general, coarse second-phase particles easily become fracture initiation sites due to stress concentration [44,45]. Additionally, second-phase particles, such as oxides and carbides, frequently contain defects, including voids and microcracks. Therefore, as the volume fraction of second-phase particles increases within the matrix, the probability of containing critical defects that can cause fractures at lower strains also increases, thereby mitigating ductility [46–48]. The frequency distribution of the oxide particle diameters shown in Fig. 3 for the Rapid-cooled and Slow-cooled samples is similar, with approximately 70 % of the measured oxide particles in both samples having diameters of 2 μm or less. Therefore, the average volume fraction of the oxide particles cannot explain the difference in ductility between the Rapid-cooled and Slow-cooled samples. Furthermore, as shown in Fig. 3, the number of the oxide particles decreases as their diameter increases in both samples, indicating that the formation of a large number of coarse oxide particles capable of acting as crack initiation sites is not limited to the Rapid-cooled sample.

4.2. The thickness and coverage rate of Nb(C, N) on the oxide particles

Thinner coatings and lower coverage rates of Nb(C, N) on oxide particles facilitate crack propagation from oxide particles, thereby reducing ductility. However, as shown in Fig. 4(a and b), the differences in these parameters between the Rapid-cooled and Slow-cooled samples are minimal. Therefore, the effect of differences in Nb(C, N) coating on the propagation behavior of cracks from oxide particles to the ferrite matrix and on resultant macroscopic ductility is likely negligible. Additionally, the higher area fraction of Nb(C, N) in the Slow-cooled sample compared to the Rapid-cooled sample can be attributed to partial dissolution of Nb(C, N) in the ferrite matrix during high-temperature holding of the as-cast specimen. This is followed by enhanced growth of plate-like Nb(C, N) during the slower cooling process. The observed trend of decreasing Nb(C, N) thickness and coverage rate with increasing oxide particle size is qualitatively explained by the greater surface area of larger oxide particles. With the same amount of solute available, the solute concentration per unit surface area decreases for larger oxide particles compared to smaller ones, resulting in thinner and less complete Nb(C, N) coatings.

4.3. Higher dislocation density around the oxide particles

During deformation, cracks generated in the oxide particles and the surrounding Nb(C, N) are expected to exhibit different propagation behavior depending on the local plastic deformation behavior around the oxide particles. Therefore, the hardness of the ferrite matrix was measured on the undeformed samples and unloaded at 10 % strain samples using nanoindentation to evaluate the local plastic deformation behavior. Fig. 12 shows the average nanohardness values at three

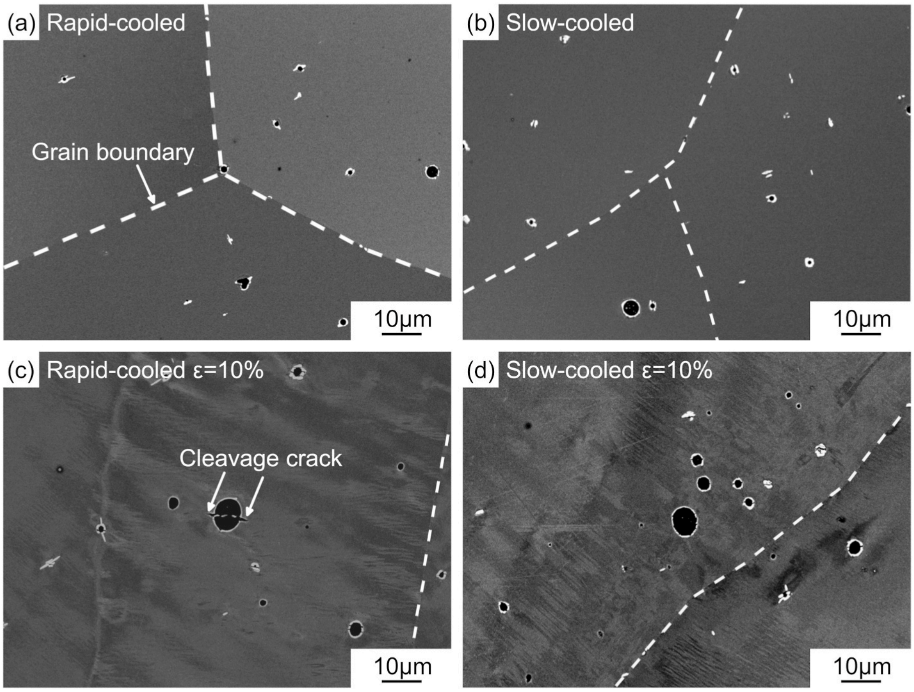

Fig. 11. SEM-BSE images of the area in the vicinity of the grain boundary for the (a, b) undeformed samples and (c, d) unloaded at 10 % strain samples with tensile direction is vertical in the images.

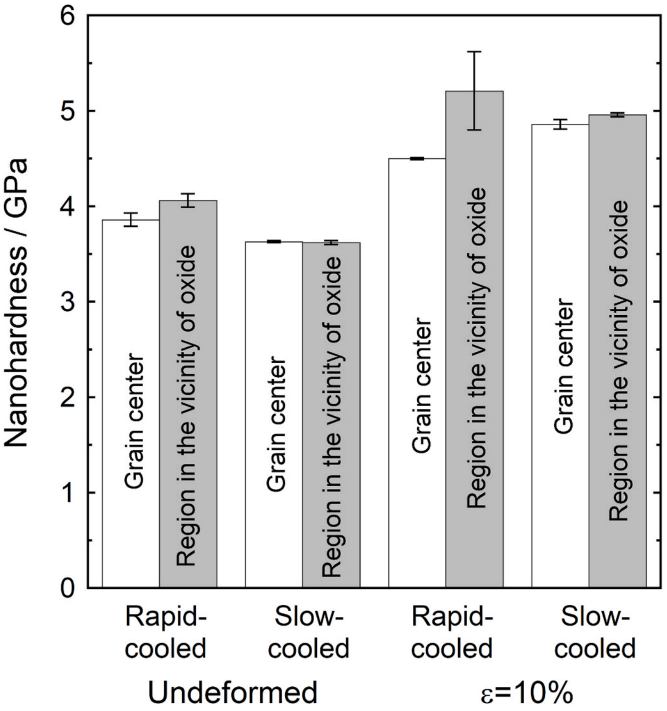

Fig. 12. Nanohardness of the undeformed sample and the sample unloaded at 10 % strain obtained by nanoindentation tests.

locations within the same grain, with 20 points measured in a grid pattern at 4 μm intervals for each location, and Fig. 13 presents the representative load-displacement curves. In the figures, “Grain center” refers to the nanoindentation results obtained in the central region of grains, at least 50 μm away from any oxide particles. “Region in the vicinity of oxide” refers to the results obtained around oxide particles (4–8 μm in diameter) coated with Nb(C, N), located within 100 μm from the grain boundaries. These measurements were performed within the area of approximately 0.5–5 μm from the interfaces between the oxide particles and the ferrite matrix, or between Nb(C, N) and the ferrite matrix. It was found from Fig. 12 that, for the undeformed Rapid-cooled samples, the nanohardness in the “Region in the vicinity of oxide” is higher than that in the “Grain center”. In contrast, the nanohardness in the “Region in the vicinity of oxide” and the “Grain center” are nearly identical for both the undeformed and 10 % strained Slow-cooled samples. The nanohardness of the “Grain center” is slightly higher in the Rapid-cooled sample than the Slow-cooled sample. The representative load-displacement curves shown in Fig. 13(a, b) indicate that distinct displacement bursts due to the pop-in phenomenon occur during the loading process for the undeformed Slow-cooled sample. In contrast, those observed in the Rapid-cooled sample are minimal. The pop-in phenomenon is attributed to the nucleation and multiplication of dislocations in regions initially free of dislocations, and it occurs more readily when the initial dislocation density is low [49–51]. Because the samples for nanoindentation experiments were prepared through mechanical and ion polishing, the influence of dislocations introduced during polishing cannot be entirely ignored. However, if the effect of polishing is comparable between the Rapid-cooled and Slow-cooled samples, the clear difference in the pop-in phenomenon can reflect differences in dislocation density of the ferrite matrix. For the Rapid-cooled sample unloaded at 10 % strain, the nanohardness in the “Region in the vicinity of oxide” is significantly higher than that in the “Grain center”. For the Slow-cooled sample unloaded at 10 % strain, the nanohardness in the “Region in the vicinity of oxide” is also higher than that in the “Grain center”, but the difference is much smaller.

Fig. 14 shows HAADF-STEM images of the (a-c) Rapid-cooled sample and (d-f) Slow-cooled sample. The sampling locations correspond to those used for the nanohardness measurements: (a, b, d, e) the regions near oxide particles coated with Nb(C, N) located within 100 μm of grain boundaries, and (c, f) the central regions of grains at least 50 μm away from any oxide particles. The observations were conducted under two-beam conditions with the diffraction vector of g* = 0 0 2, which made all perfect dislocations in bcc crystal visible, as indicated by the diffraction patterns in the upper right of Fig. 14(a–f). As shown in Fig. 14

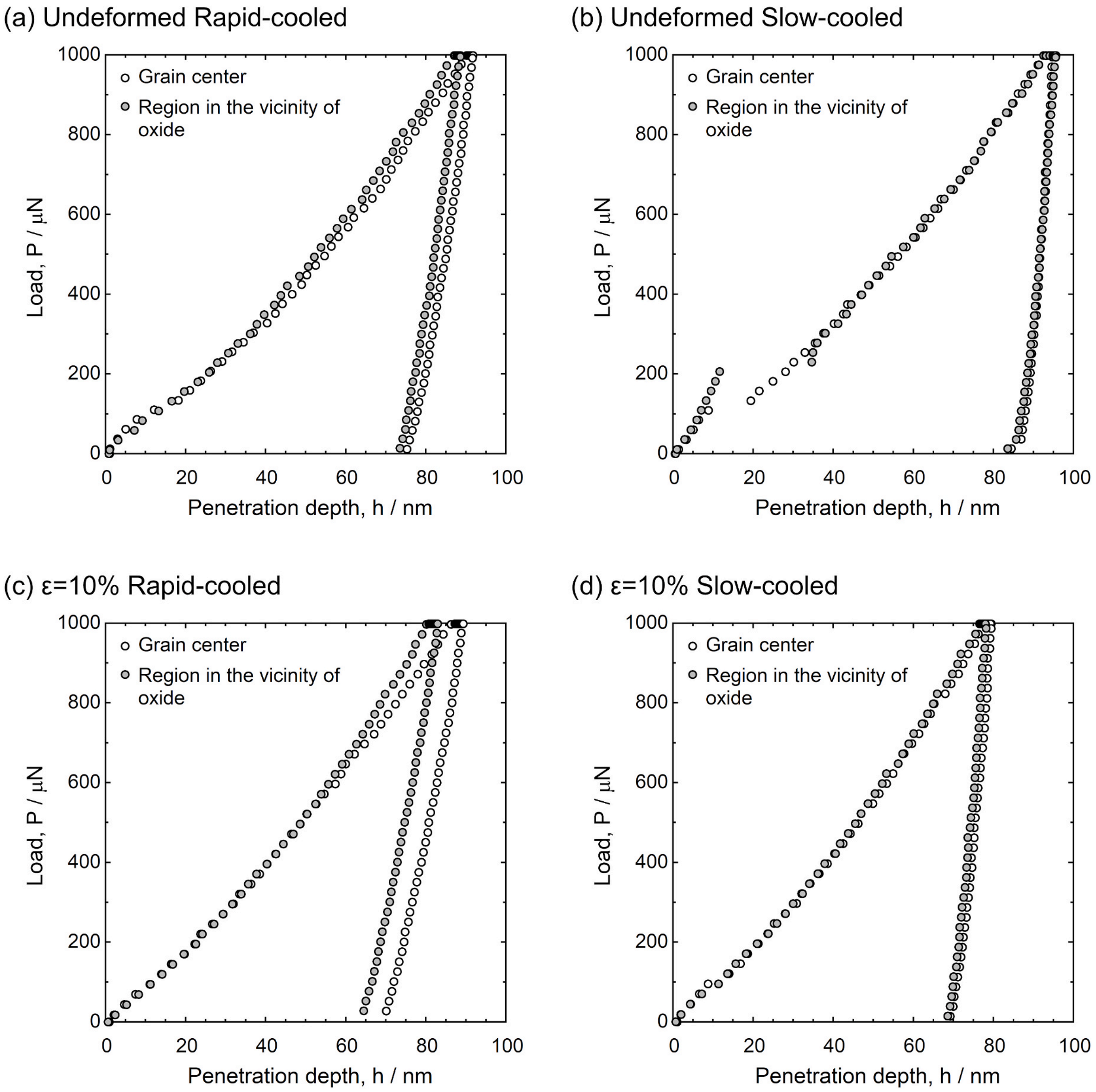

Fig. 13. Typical load-displacement curves of the undeformed sample and the sample unloaded at 10 % strain obtained by nanoindentation tests.

(a), in the Rapid-cooled sample, dislocations are observed throughout the ferrite matrix within an area of up to approximately 5 μm from the interfaces between the oxide particles and the ferrite matrix, and between Nb(C, N) and the ferrite matrix. Fig. 14(b) presents a higher magnification image of the region indicated by a rectangle in Fig. 14(a), where the dislocations near the oxide particles and Nb(C, N) appear to be intricately tangled. In contrast, as shown in Fig. 14(c), the ferrite matrix at the grain center of the Rapid-cooled sample contains fewer dislocations compared to the regions near the oxide particles. In the Slow-cooled sample, as shown in Fig. 14(d–f), dislocations are observed within approximately 1 μm from the interfaces between Nb(C, N) and the ferrite matrix. However, the number of dislocations is lower than the regions near the oxide particles in the Rapid-cooled sample (Fig. 14(a, b)). The dislocation density near the oxide particles in the Rapid-cooled sample (Fig. 14(b)) was estimated to be 8.3×10^{14} m^{-2}, while that in the Slow-cooled sample (Fig. 14(e)) was 4.2×10^{12} m^{-2}. Based on these results, the higher nanohardness surrounding oxide particles coated with Nb(C, N) in the Rapid-cooled sample, compared to the grain center, can be attributed to the higher number of dislocations introduced in these regions. Therefore, the dislocations observed near the oxide particles in Fig. 14(a, b) are likely introduced by local thermal stress generated during rapid cooling, resulting from the differences in thermal expansion coefficients among the oxide particles, Nb(C, N), and the ferrite matrix (linear expansion coefficient: 5×10^{-7}/°C, 7×10^{-6}/°C, and 11.7×10^{-6}/°C, respectively [52–54]). Although a detailed quantitative assessment of local thermal stress around the grain boundaries during cooling has not yet been performed, this remains an important topic for future investigation. However, in materials with hard second phases dispersed in a metallic matrix, it is widely known that thermal expansion coefficient differences cause strain at the interfaces between the phases during cooling, and dislocations occur when the strain exceeds the yield stress of the matrix [55,56]. Furthermore, previous studies have shown that the dislocation density increases with increasing cooling rate [57,58]. These findings are in good agreement with our experimental observations and support the interpretation that the difference in cooling rate is responsible for the dislocation density variation shown in Fig. 14. Furthermore, these dislocations likely contributed to the accumulation of dislocations around the oxide particles during the tensile deformation process, resulting in the significantly higher nanohardness in the “Region in the vicinity of oxide” compared to the “Grain center” in the Rapid-cooled sample unloaded at 10 % strain, as shown in Fig. 12.

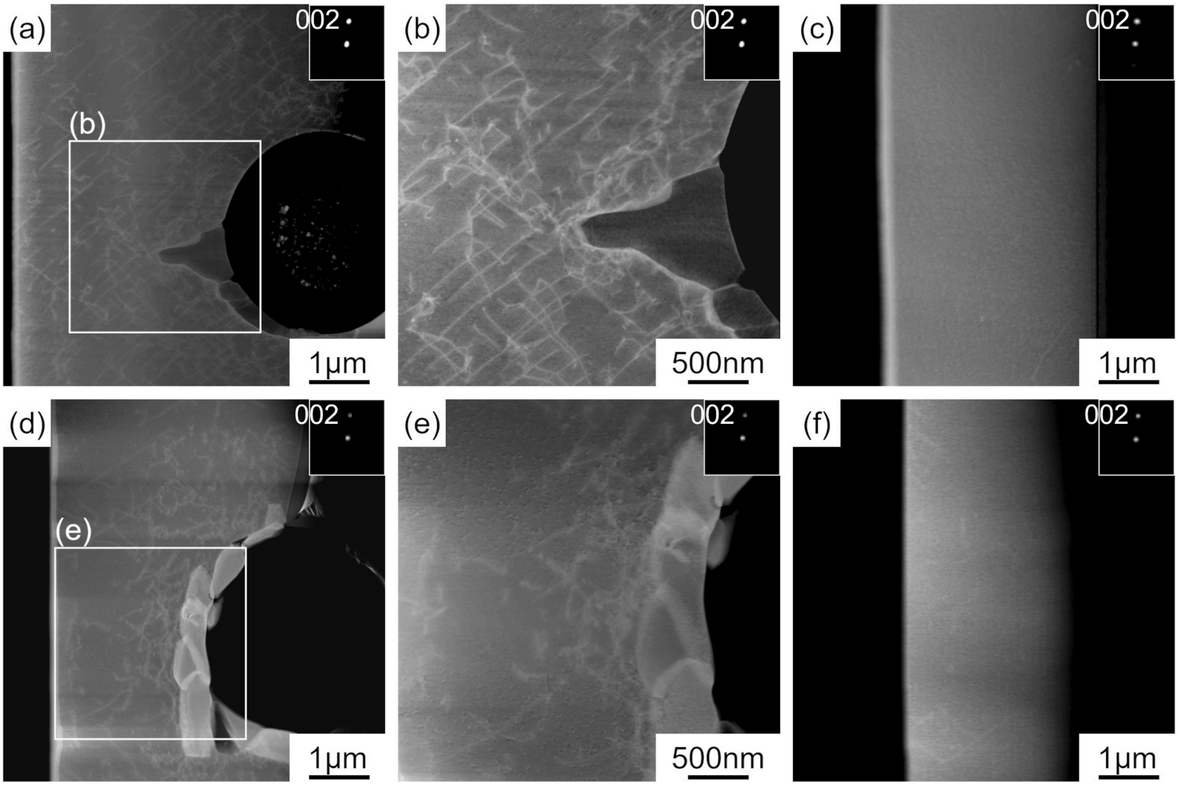

Fig. 14. HAADF-STEM images around the coarse oxide particle in the vicinity of the grain boundary and the center of the grain for the (a–c) Rapid-cooled sample, (d–f) Slow-cooled sample.

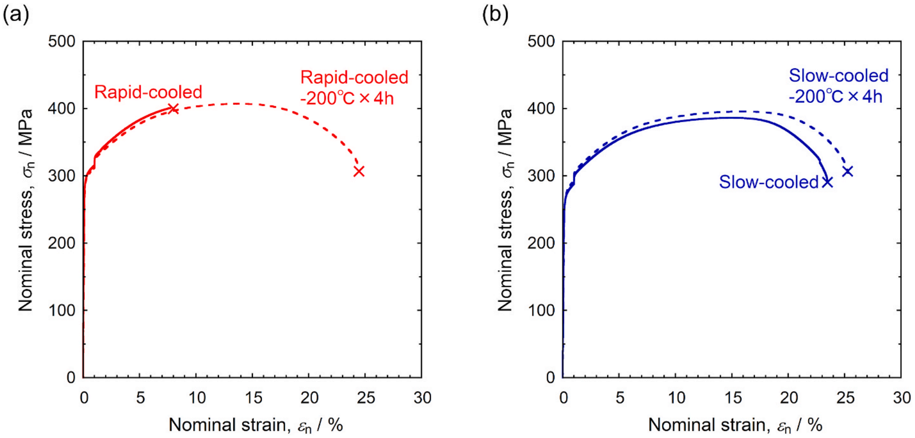

Fig. 15. Nominal stress-strain curves for the (a) Rapid-cooled sample and (b) Slow-cooled sample. The solid lines represent samples subjected to rapid cooling and slow cooling after holding at 1100 °C for 3 h, and the dashed lines represent those subjected to air cooling after annealing at 200 °C for 4 h.

In both the Rapid-cooled and Slow-cooled samples, the particle size and volume fraction of the oxide particles were similar (Fig. 3). Moreover, the differences in the thickness and coverage rate of the Nb(C, N) coating on the oxide particles were minimal (Fig. 4). Therefore, these factors can be considered negligible in terms of their effect on the ductility under different cooling rates. More importantly, a significant difference in dislocation density was observed in the regions surrounding the oxide particle. In the Rapid-cooled sample, a high density of dislocations was present around the oxide particles coated with Nb(C, N), which contributed to the increased nanohardness in that region. Furthermore, these dislocations likely enhanced stress concentration at the crack tips generated in the oxide particles and Nb(C, N) coating during tensile deformation, thereby promoting crack propagation into the ferrite matrix. In particular, near the grain boundaries with high local deformation, stress concentration around the coarse oxide particles increases, making the propagation of microcracks more likely. In contrast, the fewer dislocations around the oxide particles coated with Nb(C, N) in the Slow-cooled sample allow plastic accommodation to occur in the ferrite matrix. This reduces stress concentration around the microcracks in the Nb(C, N) and oxide particles, blunting their tips and preventing them from propagating into the ferrite matrix. To validate this consideration, we conducted tensile tests on the Rapid-cooled and Slow-cooled samples that were annealed at 200 °C for 4 h and then air cooled. The nominal stress-nominal strain curves of these specimens are shown as dashed lines in Fig. 15. The solid lines in Fig. 15 represent the nominal stress-nominal strain curves of the Rapid-cooled and Slow-cooled samples without annealing (the same as Fig. 5). The Rapid-cooled sample annealed at 200 °C exhibited a significantly higher total elongation of 24.5 % and showed sufficient local elongation (Fig. 15(a)). The total elongation of the Slow-cooled sample annealed at 200 °C also increased, but the nominal stress-nominal strain curve did not change significantly (Fig. 15(b)). In the Rapid-cooled sample, dislocations introduced around the oxide particles during rapid cooling could be annihilated and rearranged by annealing at 200 °C, resulting in the significant improvement of ductility. These results strongly support the idea that the dislocations introduced around oxide particles are one of the major factors reducing the ductility of the Rapid-cooled sample.

5. Conclusions

We investigated the influence of heat treatment on the mechanical properties of stabilized ferritic stainless cast steel. The major findings are as follows.

(1) Elongation and reduction of area increased with decreasing cooling rates. The Rapid-cooled sample (cooling rate: 2.0×10^4 °C/min) exhibited low ductility and cleavage fracture. In contrast, the Slow-cooled sample (cooling rate: 1.0 °C/min) exhibited high ductility, with ductile dimples observed on the fracture surface. These results indicate that a slower cooling rate after high-temperature holding significantly improves the ductility of the cast steel.

(2) In the Rapid-cooled sample, during plastic deformation, cracks initiated from coarse oxide particles coated with Nb(C, N) and propagated along the cleavage planes of the ferrite matrix. Cleavage cracks in the ferrite matrix were observed in the regions of high local strain near grain boundaries. Eventually, these cleavage cracks grew due to the occurrence of localized high-stress concentrations, ultimately leading to brittle fracture. In contrast, in the Slow-cooled sample, while oxide particles fractured during plastic deformation, no cracks propagating into the ferrite matrix were observed.

(3) In the ferrite matrix of the Rapid-cooled sample, the nanoindentation hardness near oxide particles coated with Nb(C, N) was higher than in the grain center, with more entangled dislocations observed. In contrast, the Slow-cooled sample exhibited similar hardness between these regions, with fewer dislocations near the oxide particles compared to the Rapid-cooled sample. These results suggest that in the Rapid-cooled sample, local thermal stress caused by differences in the thermal expansion coefficients of the ferrite matrix, oxide particles, and Nb(C, N) introduced many dislocations around oxide particles coated with Nb(C, N). We conclude that these dislocations hindered plastic accommodation around the oxide particles, leading to cleavage crack propagation in the ferrite matrix.

(4) After annealing the Rapid-cooled and Slow-cooled samples at 200 °C for 4 h followed by air cooling, the ductility of the Rapid-cooled sample significantly improved. This suggests that dislocations around oxide particles were eliminated or rearranged, confirming their role in reducing ductility.

CRediT authorship contribution statement

Rie Nishio: Writing – original draft, Visualization, Validation, Project administration, Methodology, Investigation, Formal analysis, Data curation, Conceptualization. **Takuo Umetani:** Validation, Resources, Funding acquisition, Conceptualization. **Yasuhiko Nakamura:** Resources, Funding acquisition. **Taisuke T. Sasaki:** Validation, Supervision, Resources, Methodology, Investigation, Conceptualization. **Akinobu Shibata:** Writing – review & editing, Validation, Supervision, Resources, Methodology, Investigation, Conceptualization.

Declaration of competing interest

The authors declare that they have no known competing financial interests or personal relationships that could have appeared to influence the work reported in this paper.

Acknowledgements

A part of this work was supported by Electron Microscopy Unit, Research Network and Facility Services Division, in National Institute for Materials Science (NIMS).

Data availability

Data will be made available on request.

References

[1] A.P. Gulyaev, A.N. Levanova, Brittleness of high-chromium ferritic stainless steels, Met. Sci. Heat Treat. 20 (1978) 881–886, https://doi.org/10.1007/bf00713746.

[2] M. Vardavoulias, G. Papadimitriou, D. Pantelis, Effect of $M_7C_3 \rightarrow M_{23}C_6$ transformation on fracture behaviour of cast ferritic stainless steels, Mater. Sci. Technol. 9 (8) (1993) 711–717, https://doi.org/10.1179/mst.1993.9.8.711.

[3] R.P. Siqueira, H.R.Z. Sandim, T.R. Oliveira, Texture evolution in Nb-containing ferritic stainless steels during secondary recrystallization, Mater. Sci. Eng. A 497 (1–2) (2008) 216–223, https://doi.org/10.1016/j.msea.2008.07.002.

[4] R. Li, et al., Effect of annealing treatment on microstructure, mechanical property and anti-corrosion behavior of X2CrNi12 ferritic stainless steel, J. Mater. Res. Technol. 18 (2022) 448–460, https://doi.org/10.1016/j.jmrt.2022.02.117.

[5] Y. Zhao, et al., Overview Novel Heat Resistant Ferritic Stainless Steels (2023) 467–480, https://doi.org/10.1007/s42864-022-00171-4. Tungsten 5.4.

[6] W. Gordon, A. van Bennekom, Review of stabilisation of ferritic stainless steels, Mater. Sci. Technol. 12 (2) (1996) 126–131, https://doi.org/10.1179/mst.1996.12.2.126.

[7] N. Fujita, et al., Effect of Nb on high-temperature properties for ferritic stainless steel, Scr. Mater. 35 (6) (1996) 705–710, https://doi.org/10.1016/1359-6462(96)00214-X.

[8] N. Fujita, K. Ohmura, A. Yamamoto, Changes of microstructures and high temperature properties during high temperature service of Niobium added ferritic stainless steels, Mater. Sci. Eng. A 351 (1–2) (2003) 272–281, https://doi.org/10.1016/S0921-5093(02)00831-6.

[9] J.L. Cavazos, Characterization of precipitates formed in a ferritic stainless steel stabilized with Zr and Ti additions, Mater. Char. 56 (2) (2006) 96–101, https://doi.org/10.1016/j.matchar.2005.05.006.

[10] J. Hamada, C. Takushima, Effect of initial grain size on thermal fatigue behavior and changes in microstructure of ferritic stainless steel, Mater. Trans. 60 (5) (2019) 743–750, https://doi.org/10.2320/matertrans.M2018382.

[11] E. Zhu, et al., Study on the effect of niobium on the high temperature oxidation resistance of ferritic stainless steel, JMET (J. Med. Eng. Technol.) 14 (1) (2023) 25, https://doi.org/10.3390/met14010025.

[12] J. Zheng, Y. Zhao, L. Chen, High-temperature precipitation behavior of W-containing 444-type ferritic stainless steel in a simulated cyclic annealing process, J. Mater. Res. Technol. 26 (2023) 1712–1722, https://doi.org/10.1016/j.jmrt.2023.07.189.

[13] G.M. Sim, et al., Effect of Nb precipitate coarsening on the high temperature strength in Nb containing ferritic stainless steels, Mater. Sci. Eng. A 396 (1–2) (2005) 159–165, https://doi.org/10.1016/j.msea.2005.01.030.

[14] H. Yan, et al., Microstructure and texture of Nb + Ti stabilized ferritic stainless steel, Mater. Char. 59 (12) (2008) 1741–1746, https://doi.org/10.1016/j.matchar.2008.03.018.

[15] J.F. Almagro, et al., Soluble fraction of stabilising elements in ferritic stainless steel, Microchim. Acta 161 (2008) 323–327, https://doi.org/10.1007/s00604-007-0925-6.

[16] L. Jacquet, et al., Study of cleavage fracture in ferritic stainless steels part I: development and characterization of model microstructures, Mater. Sci. Eng. A 864 (2023) 144534, https://doi.org/10.1016/j.msea.2022.144534.

[17] S. Jones, C. Yuan, Advances in shell moulding for investment casting, J. Mater. Process. Technol. 135 (2–3) (2003) 258–265, https://doi.org/10.1016/S0924-0136(02)00907-X.

[18] S. Pattnaik, D.B. Karunakar, P.K. Jha, Developments in investment casting process—A review, J. Mater. Process. Technol. 212 (11) (2012) 2332–2348, https://doi.org/10.1016/j.jmatprotec.2012.06.003.

[19] Z. Xiao, et al., Numerical simulation and optimization of investment casting for complex thin-walled castings, Int. J. Metalcast. 18 (1) (2024) 159–179, https://doi.org/10.1007/s40962-023-00990-2.

[20] M. Flemings, Solidification processing, Metall. Trans. A 5 (10) (1974) 2121–2134, https://doi.org/10.1007/bf02643923.

[21] A. Nazarboland, R. Elliott, The effect of intrinsic casting defects on the mechanical properties of austempered, alloyed ductile iron, Int. J. Cast Met. Res. 10 (2) (1997) 87–97, https://doi.org/10.1080/13640461.1997.11819223.

[22] G. Krauss, Solidification, segregation, and banding in carbon and alloy steels, Metall. Mater. Trans. B 34 (6) (2003) 781–792, https://doi.org/10.1007/s11663-003-0084-z.

[23] J. Han, et al., Effects of processing optimisation on microstructure, texture, grain boundary and mechanical properties of Fe–17Cr ferritic stainless steel thick plates, Mater. Sci. Eng. A 616 (2014) 20–28, https://doi.org/10.1016/j.msea.2014.07.107.

[24] X. Liu, et al., Enhancing mechanical properties of twin-roll cast al–mg–si–fe alloys by regulating Fe-bearing phases and macro-segregation, Mater. Sci. Eng. A 831 (2022) 142256, https://doi.org/10.1016/j.msea.2021.142256.

[25] P. Rawat, U. Prakash, V.V.S. Prasad, Microstructure and mechanical behaviour of Nb-containing high Al ferritic low density steels, Mater. Char. 204 (2023) 113176, https://doi.org/10.1016/j.matchar.2023.113176.

[26] R. Nishio, et al., Effect of Nb content on mechanical properties and solidification microstructure of stabilized ferritic stainless cast steel, Mater. Trans. 66 (1) (2025) 99–106, https://doi.org/10.2320/matertrans.F-M2024812.

[27] M. Torkar, F. Vodopivec, S. Petovar, Analysis of segregations in as-cast X40CrMoV51 steel, Mater. Sci. Eng. A 173 (1–2) (1993) 313–316, https://doi.org/10.1016/0921-5093(93)90235-7.

[28] Y. Han, et al., Dendrite segregation changes in high temperature homogenization process of as-cast H13 steel, ISIJ Int. 59 (10) (2019) 1893–1900, https://doi.org/10.2355/isijinternational.ISIJINT-2019-148.

[29] D. Li, C. Sloss, Heat treatment of heat-resistant ferrous cast alloys, Int. J. Med. 9 (2015) 7–20, https://doi.org/10.1007/BF03355611.

[30] W.L. Gao, et al., Effects of niobium and heat treatment on microstructure and mechanical properties of low carbon cast steels, Mater. Des. 105 (2016) 114–123, https://doi.org/10.1016/j.matdes.2016.05.057.

[31] J. Zhao, et al., Enhancing mechanical properties of a low-carbon microalloyed cast steel by controlled heat treatment, Mater. Sci. Eng. A 559 (2013) 427–435, https://doi.org/10.1016/j.msea.2012.08.122.

[32] A. Xie, et al., Homogenization temperature dependent microstructural evolution and mechanical properties in a Nb-stabilized cast austenitic stainless steel, Mater. Char. 194 (2022) 112384, https://doi.org/10.1016/j.matchar.2022.112384.

[33] Y. Hu, et al., Effect of normalizing treatment on mechanical properties of AISI 441 stainless steel prepared by investment casting, JMET (J. Med. Eng. Technol.) 11 (3) (2021) 474, https://doi.org/10.3390/met11030474.

[34] Y. Kang, et al., Influence of Nb content on grain size and mechanical properties of 18 wt% Cr ferritic stainless steel, Mater. Sci. Eng. A 677 (2016) 453–464, https://doi.org/10.1016/j.msea.2016.09.080.

[35] N. Saunders, A.P. Miodownik (Eds.), CALPHAD (Calculation of Phase Diagrams): a Comprehensive Guide, Elsevier, 1998.

[36] N.J. Petch, The fracture of metals, Prog. Met. Phys. 5 (1954) 1–52, https://doi.org/10.1016/0502-8205(54)90003-9.

[37] M.F. Ashby, Work hardening of dispersion-hardened crystals, Philos. Mag. 14.132 (1966) 1157–1178, https://doi.org/10.1080/14786436608224282.

[38] T. Goldenberg, T.D. Lee, J.P. Hirth, Ductile fracture of U-notched bend specimens of spheroidized AISI 1095 steel, Metall. Trans. A 9 (1978) 1663–1671, https://doi.org/10.1007/bf02661950.

[39] P.J. Noell, et al., Void nucleation during ductile rupture of metals: a review, Prog. Mater. Sci. 135 (2023) 101085, https://doi.org/10.1016/j.pmatsci.2023.101085.

[40] A. Argon, J. Im, R. Safoglu, Cavity formation from inclusions in ductile fracture, Metall. Trans. A 6 (1975) 825–837, https://doi.org/10.1007/bf02672306.

[41] R. Thomson, J.W. Hancock, Ductile failure by void nucleation, growth and coalescence, Int. J. Fract. 26 (1984) 99–112, https://doi.org/10.1007/bf01157547.

[42] R.H.V. Stone, et al., Microstructural aspects of fracture by dimpled rupture, Int. Met. Rev. 30 (1) (1985) 157–180, https://doi.org/10.1179/imtr.1985.30.1.157.

[43] S.J. Goodwin, F.W. Noble, B.L. Eyre, Inclusion nucleated ductile fracture in stainless steel, Acta Metall. 37 (5) (1989) 1389–1398, https://doi.org/10.1016/0001-6160(89)90170-3.

[44] T.B. Cox, J.R. Low, An investigation of the plastic fracture of AISI 4340 and 18 Nickel-200 grade maraging steels, Metall. Mater. Trans. B 5 (1974) 1457–1470, https://doi.org/10.1007/bf02646633.

[45] P. Bowen, S.G. Druce, J.F. Knott, Effects of microstructure on cleavage fracture in pressure vessel steel, Acta Metall. 34 (6) (1986) 1121–1131, https://doi.org/10.1016/0001-6160(86)90222-1.

[46] D.A. Curry, J.F. Knott, Effects of microstructure on cleavage fracture stress in steel, Met. Sci. 12 (11) (1978) 511–514, https://doi.org/10.1179/msc.1978.12.11.511.

[47] W.M. Garrison, A.L. Wojcieszynski, A discussion of the spacing of inclusions in the volume and of the spacing of inclusion nucleated voids on fracture surfaces of steels, Mater. Sci. Eng. A 505 (1–2) (2009) 52–61, https://doi.org/10.1016/j.msea.2008.11.065.

[48] J.J. Williams, et al., Damage evolution in SiC particle reinforced Al alloy matrix composites by X-ray synchrotron tomography, Acta Mater. 58 (18) (2010) 6194–6205, https://doi.org/10.1016/j.actamat.2010.07.039.

[49] A. Gouldstone, K. Van Vliet, S. Suresh, Simulation of defect nucleation in a crystal, Nature 411 (6838) (2001), https://doi.org/10.1038/35079687, 656-656.

[50] T. Ohmura, K. Tsuzaki, S. Matsuoka, Evaluation of the matrix strength of Fe-0.4 wt % C tempered martensite using nanoindentation techniques, Philos. Mag. A 82 (10) (2002) 1903–1910, https://doi.org/10.1080/01418610210135070.

[51] A.A. Zbib, D.F. Bahr, Dislocation nucleation and source activation during nanoindentation yield points, Metall. Mater. Trans. A 38 (2007) 2249–2255, https://doi.org/10.1007/s11661-007-9284-5.

[52] P.H. Gaskell, Thermal properties of silica. Part 2.-Thermal expansion coefficient of vitreous silica, Trans. Faraday Soc. 62 (1966) 1505–1510, https://doi.org/10.1039/tf9666201505.

[53] R.O. Elliott, C.P. Kempter, Thermal expansion of some transition metal carbides, J. Phys. Chem. 62 (5) (1958) 630–631, https://doi.org/10.1021/j150563a030.

[54] H. Masumoto, S. Sawaya, M. Kikuchi, Thermal expansion and temperature dependence of young's modulus in Fe–Cr alloys, Trans. Jpn. Inst. Met. 12 (2) (1971) 86–89, https://doi.org/10.2320/matertrans1960.12.86.

[55] R.J. Arsenault, N. Shi, Dislocation generation due to differences between the coefficients of thermal expansion, Mater. Sci. Eng. 81 (1986) 175–187, https://doi.org/10.1016/0025-5416(86)90261-2.

[56] B. Zhang, et al., Achieving high strength-ductility combination and negligible yield asymmetry in extruded AlN/AZ91 composite rods, Mater. Sci. Eng. A 773 (31) (2020) 138842, https://doi.org/10.1016/j.msea.2019.138842.

[57] C. Wang, et al., Decreased dislocation density as an origin for the quench sensitivity of the Al-Si-Mg alloys with high Si content, J. Alloys Compd. 910 (25) (2022) 165011, https://doi.org/10.1016/j.jallcom.2022.165011.

[58] J. Chen, et al., Effect of cooling rate on microstructure evolution and mechanical properties of SCM435 steel, Metals 14 (2) (2024) 140, https://doi.org/10.3390/met14020140.